# Wind Tunnel Validation of a Particle Tracking Model to Evaluate the Wind-Induced Bias of Precipitation Measurements.

Arianna Cauteruccio[1], Elia Brambilla[2], Mattia Stagnaro[3], Luca Giovanni Lanza[1], and Daniele Rocchi[2]

[1]University of Genova
[2]Department of Mechanical Engineering, Politecnico di Milano, Milan, Italy
[3]Department of Civil, Chemical and Environmental Engineering, University of Genova, Genoa, Italy

November 23, 2022


## Abstract

A physical full-scale experimental set-up was designed and implemented in the wind tunnel to reproduce and capture the trajectories of falling water drops when approaching the collector of catching type precipitation gauges, reproducing rainfall measurements in windy conditions. The experiment allowed to collect, for the first time, a large dataset of high-resolution footages of the deviation of such trajectories, as induced by the bluff-body aerodynamics of the outer gauge shape. By processing the collected images, a consistent quantitative interpretation of each drop pattern was possible, based on a detailed Computational Fluid Dynamics simulation of the airflow updraft and acceleration features above the collector of the gauge. Numerical airflow simulations were extensively validated in the wind tunnel, using local flow measurements and Particle Image Velocimetry. Capturing the deviation of the drop trajectories in the wind tunnel allowed a clear visualisation of the physical reason for the wind-induced undercatch of precipitation gauges, since drops were individually observed to fall outside instead of inside of the collector, contrary to what would be expected by extrapolating their undisturbed trajectory. The adopted Lagrangian Particle Tracking model and the formulation used for the drag coefficient were suitable to closely reproduce the observed drop trajectories when affected by the airflow deformation due to the bluff-body aerodynamics of two investigated gauge geometries. The wind tunnel experiment provided the basis for the validation of the particle tracking model in terms of the difference between simulated and observed trajectories, after initial conditions were suitably set to represent the experimental setup.

# Wind Tunnel Validation of a Particle Tracking Model to Evaluate the Wind-Induced Bias of Precipitation Measurements

**A. Cauteruccio[1], E. Brambilla[2], M. Stagnaro[1], L. G. Lanza [1,3] and D. Rocchi[2]**

[1]Department of Civil, Chemical and Environmental Engineering, University of Genova, Genoa, Italy

[2]Department of Mechanical Engineering, Politecnico di Milano, Milan, Italy

[3]WMO/CIMO Lead Centre "B. Castelli" on Precipitation Intensity, Italy

Corresponding author: Luca G. Lanza (luca.lanza@unige.it)

**Key Points:**

- Water drops are released in a wind tunnel to mimic rainfall and tracked to observe the wind-induced measurement bias of raingauges
- Numerical simulation of the airflow field and a lagrangian particle tracking model are applied to reproduce the drop trajectories
- Wind tunnel tests validate airflow simulation and particle tracking results supporting their application in studying the wind-induced bias

## Abstract

A physical full-scale experimental set-up was designed and implemented in the wind tunnel to reproduce and capture the trajectories of falling water drops when approaching the collector of catching type precipitation gauges, reproducing rainfall measurements in windy conditions. The experiment allowed to collect, for the first time, a large dataset of high-resolution footages of the deviation of such trajectories, as induced by the bluff-body aerodynamics of the outer gauge shape. By processing the collected images, a consistent quantitative interpretation of each drop pattern was possible, based on a detailed Computational Fluid Dynamics simulation of the airflow updraft and acceleration features above the collector of the gauge. Numerical airflow simulations were extensively validated in the wind tunnel, using local flow measurements and Particle Image Velocimetry. Capturing the deviation of the drop trajectories in the wind tunnel allowed a clear visualisation of the physical reason for the wind-induced undercatch of precipitation gauges, since drops were individually observed to fall outside instead of inside of the collector, contrary to what would be expected by extrapolating their undisturbed trajectory. The adopted Lagrangian Particle Tracking model and the formulation used for the drag coefficient were suitable to closely reproduce the observed drop trajectories when affected by the airflow deformation due to the bluff-body aerodynamics of two investigated gauge geometries. The wind tunnel experiment provided the basis for the validation of the particle tracking model in terms of the difference between simulated and observed trajectories, after initial conditions were suitably set to represent the experimental setup.


## 1 Introduction

The external design of catching type precipitation gauges has a major impact on the catch efficiency in windy conditions due to the bluff-body aerodynamics of their outer geometry. This topic is numerically investigated by using Computational Fluid Dynamics (CFD) simulations of the airflow field surrounding the gauge body (see e.g. Colli et al., 2018) and by adopting a Lagrangian Particle Tracking (LPT) model to evaluate the airflow induced deformation on the trajectory of the approaching hydrometeors (see e.g. Nešpor & Sevruk, 1999).

The work of Mueller & Kidder (1972) is among the earliest studies on the modelling of hydrometeor trajectories using a LPT model; in that work, particle trajectories were numerically simulated based on the flow field measured in the wind tunnel (WT) employing hot film anemometers. Folland (1988) later developed two simplified trajectory models to estimate the catch losses due to the wind. They were based on flow patterns (flow velocity and direction) obtained in the vertical section along the symmetry axis in the streamwise direction partially published by Robinson & Rodda (1969), and the flow field close to the windward edge as described in the work of Warnik (1953). In the first model, a two-dimensional solution was obtained by simulating one by one droplets of fixed diameter until the expected drop size distribution was generated. Then the model was extended to a three-dimensional domain by considering the variation of the gauge orifice width in the transversal direction. The second model, which the author terms "semi-analytical", uses geometrical considerations to calculate the number of particles which fall outside instead of inside of the gauge collector.

In the work of Nešpor & Sevruk (1999), the airflow velocity field around three cylindrical gauges characterized by different shapes of the collector rim was calculated by numerically solving the Reynolds Average Navier-Stokes (RANS) equations based on the k-ε turbulence closure model. Then, liquid particle trajectories were modelled by employing a one-way coupled model where spherical particles are separately simulated for each diameter and the Collection Efficiency (CE) is evaluated by computing the integral, over the particle size distribution, of the number of particles collected by the gauge with respect to the total precipitation. This simulation scheme was also adopted by Thériault et al. (2012) and Colli et al. (2015, 2016 a,b) for solid precipitation, by increasing the details of the computational mesh to better capture the airflow features and using also Large Eddy Simulations (LES). In the work of Thériault et al. (2012) different crystal types were modelled by using a power law parametrization of the terminal velocity, volume, density and cross section of the particles, while Colli *et al.* (2016b) investigated two macro categories: wet and dry snow as suggested by Rasmussen et al. (1999). In these works, a fixed drag coefficient for each crystal type was adopted. In the work of Colli et al. (2016b) the obtained collection efficiency curves for the two macro categories act as upper and lower thresholds of the wide spreading of experimental data. Colli et al. (2015) obtained a better comparison with real-world data by introducing the dependence of the aerodynamic Drag Coefficient ( $C_D$) on the local Reynolds number of the simulated particle ($Re_p$). The $Re_p$ is function of the instantaneous particle-to-air magnitude of velocity and the particle trajectory is obtained by updating its value and the associated $C_D$ at each simulation time step.

Due to the difficulties in reproducing hydrometeors trajectories under controlled WT conditions, or to observe their deflection when approaching the gauge in any real world configuration, the validation of trajectory models is scarcely documented yet in the literature. Very few literature works, Warnik (1953) and Green & Helliwell (1972), report some attempts to detect water drops in WT.

The WT experiments performed by Warnik (1953) were a pioneer work where the trajectories of precipitating solid particles under windy conditions and their deviations when approaching the gauge were first visualized. However, no attempt to quantitatively measure and model the deviation of particles in the presence of the gauge collector was made and just the overall undercatch was quantitatively obtained. The main objective was to define the air-flow behavior around the investigated gauges and to give definite information about the inconsistencies observed in records of snow catch in precipitation gauges. Results were used to design the geometry of two windshields with better performance than the shields in use at that time. Green & Helliwell (1972) measured wind velocity profiles and raindrop trajectories above a cylindrical rain gauge in a WT. The flow field was measured using a grid of hotwire anemometers and the trajectories of injected drops using photographs from a still reflex camera. Furthermore, they simulated the drop trajectories based on the streamlines obtained by visually interpreting the pattern of smoke injected in the WT. Little details are provided about the algorithms and procedures used in that work.

The original contribution of the present work consists of a dedicated WT experimental setup, where a physical full-scale model was designed and realized in order to release water drops in the WT flow field and to detect – at high resolution – their deviated trajectories close to the gauge collector, where the airflow field is modified by the presence of the gauge body.

Dedicated numerical simulation of the experimental setup was performed by adapting the CFD approach proposed by Nešpor & Sevruk (1999), Thériault et al. (2012) and Colli et al. (2016 a) and implementing the LPT model with suitable initial conditions (drop velocity and position), as observed in the WT. The improved LPT model used by Colli et al. (2015) for solid precipitation was adapted to simulate the trajectories of water droplets when falling through the atmosphere and approaching the gauge collector using suitable drag coefficient equations as a function of the local Reynolds number of the simulated particles. Comparison between the simulated and observed trajectories of droplets of various size and fall height allowed full validation of the LPT model in a controlled WT environment.

## 2 Methodology

The most popular outer shapes of catching type precipitation gauges, cylindrical and chimney-shaped (or conical), were investigated. Although actually exploiting a weighing measurement principle, the *Lambrecht Rain[e]H3*© precipitation gauge has a cylindrical outer shape (see Figure 1 top-left) and is assumed here as representative of the majority of tipping-bucket gauges, while the *Geonor T200B*© has a chimney shape (see Figure 1 bottom-left) that is typical of most weighing type gauges.

Within the *PRIN 20154WX5NA* project, an extensive experimental campaign was conducted in the WT facility available at Politecnico di Milano, hereafter GVPM, and in the WT of the DICCA department at the University of Genova. This included Particle Image Velocimetry (PIV) and local flow velocity measurements, and the release and tracking of droplets using a drop generator and a high-speed camera.

### 2.1 Wind Tunnel experiments

The numerical velocity fields were validated by comparison with PIV measurements along two vertical sections in the 2-D ($x$, $z$) plane, where $x$ is the stream-wise direction, above the *Geonor T200B*© collector and with local flow velocity measurements obtained in selected positions close to the *Lambrecht Rain[e]H3*© collector.

For PIV measurements, the GVPM test chamber was uniformly filled with castor oil smoke, used as a tracer. A laser emitter was mounted on the ceiling of the test chamber to illuminate the measurement plane, while the surrounding environment was kept in the dark. The video camera was positioned with its central axis normal to the stream-wise direction and centered on the transversal symmetry axis of the collector of the *Geonor T200B*©. Post processing of the acquired images provided the flow velocity field discretized in a regular grid with cell size of 7.5 x 7.5 mm. Part of the data, acquired very close to the gauge surface and disturbed by the reflection of the laser beam on the gauge rim, were masked out.

The *Lambrecht Rain[e]H3*© precipitation gauge was tested in the DICCA WT. Local measurements of the wind speed were acquired using a fast-response multi-hole probe, the "*Cobra*" probe, characterized by an measuring cone of $\pm 45°$, mounted on a 3 degrees of freedom traversing system. Each measurement was sampled at 2 kHz for 30 seconds. The measurement positions were selected above the gauge along two longitudinal lines at different elevations and along two vertical lines at the center and the upwind edge of the collector.

With the aim to validate the LPT model, water drops were injected in the GVPM WT and their trajectories were captured with a high-speed camera in the vertical 2-D plane along the main flow direction. The deviation of the drop trajectories approaching and travelling above the gauge collector was measured. The WT was equipped with a hydraulic system to generate water droplets, a high-speed camera and a high-power lamp to photograph and illuminate the droplets along their trajectories. The experimental setup is illustrated in the right panel of Figure 1. The hydraulic system consisted of a tank with a constant water head, feeding a volumetric pump

(Ismatec Reglo-Z digital) connected to a calibrated nozzle; the droplets releasing frequency could be adjusted by varying the pump flow rate between 0.4 and 18.0 ml/min. Tests were conducted using a fixed flow rate of 0.8 ml/min and a nozzle orifice size of 0.008''. The support for the nozzle was shaped to have a reduced impact on the airflow close to the orifice and to minimize the oscillations at the edge where droplets are released.

**Figure 1.** Lambrecht Rain[e]H3© (top-left) and Geonor T200B© (bottom-left) precipitation gauges and experimental setup to release drops and photograph their trajectories installed in the GVPM.

The high-speed camera was placed in front of the gauge and its distance from the gauge collector was optimized to increase the resolution of the captured drop images without affecting the airflow field near the target. The focus plane was set as the vertical section along the streamwise symmetry axis of the gauge collector. Acquisition of video sequences was carried out at both a high-frame rate (fps) and a low-frame rate. In the first case, the recording speed was optimized to maintain high quality of the images, in terms of resolution and luminosity, suitable for capturing the drop movement with no streaks appearing due to an excessive exposure time with respect to the drop displacement. The recording speed was set to 1000 fps, with an image resolution of 1600x900 pixels. During the low frame rate acquisition, the recording speed was kept low, 10 fps with the same image resolution, in order to increase the exposure time. In this way the trajectory of a bright moving object was imprinted in a single image in the form of a single streak.

The GVPM WT campaign was realized in subsequent time slots, in each of them the dimension of the image was about 40 x 20 cm with the pixel size equal to 0.2370 mm for the *GeonorT200B*© gauge and 0.2424 mm for the for *Lambrecht Rain[e]H3*©. The wind speed range investigated was between 9 and 13 m $s^{-1}$. The lighting was designed to increase the drops visibility in the videos: an incandescent lamp was used to illuminate the volume near the gauge collector. Tests were conducted in a dark environment while backlighting the gauge from above using the lamp. The lamp lights are suitably directed to avoid the saturation of the recorded videos.

The investigated precipitation gauges were positioned downstream of the drop generator, so that drops were released along the streamwise symmetry axis of the gauge. The drop release position was determined a priori using the LPT model based on the flow field provided by CFD simulations at a wind speed equal to 10 m s$^{-1}$. The drop size was set equal to the minimum dimension that the video camera is able to capture (1 mm) following dedicated tests performed in still air. The initial velocity of the drop was imposed equal to zero in all directions. This configuration allowed a significant deformation of the trajectories to be observed when drops travelled in the region where the flow field is disturbed by the presence of the gauge. This configuration was chosen since drops could not be generated with their terminal velocity, otherwise – given the above mentioned constraints on the drop size – the high inertia of such large drops would have resulted into an imperceptible deflection of the drop trajectories above the gauge collector.

The videos recorded by the camera were imported and analyzed in the MATLAB® environment. The methodology of detection of the drop position differs depending on the type of acquisition. In high-fps, the path of each drop is identified by many frames: in every frame the drop is in a different position. Due to the reduced exposure time of each image, little light enters into the camera sensor and the image is dark. To improve the drop position identification, each image was then converted to greyscale and a combination of a Gaussian and Laplacian filter was applied. The image was binarized using a threshold level, with the zeroes indicating the background color while the ones indicate the drop position. Finally, using a moving window over the image, the center of the drop was identified and stored. Knowing the time interval between two subsequent images and the conversion rate from pixels to mm, it was also possible to calculate the drop speed in the 2-D shooting plane. In low-fps acquisition, due to the high exposure time, every frame appears much more bright and contains a streak representing the trajectory of each single drop. The same filtering and binarization operations were used, adapting the filter and threshold parameters. Finally, morphological operations were carried out, in order to extract from the image the middle line streak, directly corresponding to the trajectory of the drop.

## 2.2 CFD simulations

To obtain the modified airflow velocity fields (magnitude and components) around the two investigated gauges, CFD simulations were performed under constant wind velocity and uniform incoming free-stream conditions. First, an Unsteady Reynolds Average Navier-Stokes (URANS) model was applied to the simulation of the flow field around the *Geonor T200B*© gauge geometry in order to check the occurrence of any variation in time of the average velocity field. Results revealed that a steady state solution is reached in the region of major interest for this work, i.e. above the gauge collector, and only beyond the gauge, in the wake, a time dependent solution persists. For this reason, in order to reduce the computational burden, a RANS model was used in the simulation of the *Lambrecht Rain[e]H3*© gauge. In both cases, the SST (Shear Stress Transport) k-ω turbulence model, based on the (specific) turbulence kinetic energy ($k$), the energy dissipation per unit mass ($\varepsilon$) and the turbulent specific dissipation rate ($\omega$) as defined in Wilcox (2006), was adopted. The SST k-ω closure model was developed by Menter (1992) and concentrates the advantages of the more classic $k$-$\varepsilon$ and $k$-$\omega$ models because it is able to switch to a k-ε behaviour in the free stream far from the object and to the $k$-$\omega$ model near the walls. Indeed, the $k$-$\varepsilon$ model formulated by Jones & Launder, (1973), is robust and reliable in the free flow region but it proved to be unreliable near the boundary layer, while the k-ω model formulated by Wilcox (1988) is capable of correctly modelling turbulence near the boundary layer, though presenting a strong dependency on arbitrary values in the free flow. Concerning the topic of this work, Constantinescu et al. (2007) tested different numerical methods to investigate the shielding problem between two contiguous precipitation gauges, and concluded that the SST k-ω model is more consistent with the time-dependent LES results on the upstream gauge, in conditions that are similar to the present work.

Although it was demonstrated (Cauteruccio et al., 2020) that the free-stream turbulence intensity inherent to the natural wind has a significant role in attenuating the aerodynamic effect of precipitation gauges, due to the energy dissipation induced by turbulent fluctuations, in this work a low free-stream turbulence condition was used to reproduce the WT environment where the particle tracking experiment was carried out.

To prepare the simulation setup, first the numerical models of the gauge geometries were realized in the Standard Triangulation Language (STL) format using a 3D CAD software. The three-dimensional computational spatial domains were discretized using an unstructured hybrid hexahedral/prismatic finite volume mesh. The number of cells of the computational mesh is 1.5 x $10^6$ for the *Geonor T200B*© and doubled for the *Lambrecht Rain[e]H3*© due to the sharp edge that characterized the rim geometry, which requires an accurate discretization. In both cases, mesh refinement boxes and thin layers were realized close to the gauge and on its surface in order to increase the accuracy of the numerical solution in the region affected by large gradients of velocity and pressure. The quality of the mesh was checked by using the geometry parameters of orthogonality, skewness and aspect ratio.

The open-source OpenFOAM software was employed to solve the URANS and RANS equations. The fluid air was modelled as a Newtonian incompressible fluid with kinematic viscosity $\nu_a$ = 1.5 x $10^{-5}$ $m^2s^{-1}$ and density $\rho_a$ = 1.25 kg $m^{-3}$ at a reference environmental temperature $T_a$ = 20 °C. For each configuration, at the inlet of the computational domain (*y-z* plane) the undisturbed wind speed, $U_{ref}$, equal to 10 $ms^{-1}$ was imposed parallel to the *x* axis and it was maintained uniform and constant in time, while a null gradient condition was set for pressure. At the outlet, *y-z* plane opposite to the inlet, the atmospheric pressure and a null gradient condition for the velocity were imposed. The lateral surfaces of the domain were set as symmetry planes, while the ground and the gauge surface were assumed impermeable with a no-slip condition. In all computational cells, initial conditions were imposed equal to $U_{ref}$ for the velocity and equal to zero for the relative pressure.

### 2.3 The Lagrangian Particle Tracking model

The LPT model used by Colli et al. (2015) for solid precipitation was modified by introducing drag coefficient equations suitable for liquid precipitation. Drop trajectories were computed with a forward step procedure by calculating at short time intervals the particle position, velocity and acceleration. The relative particle-to-air velocity was updated at every time step by interpolating the CFD airflow field to obtain the flow velocity in the exact position of the drop. This model is one-way coupled since the potential influence of the particles on the airflow field is neglected. This simplification is acceptable since the particles concentration in the air is very low as observed by Cauteruccio (2020). A spherical shape was assumed for the water drops, with the associated equivalent diameter *d*, and the particle density was set equal to 1000 kg $m^{-3}$ at the air temperature of 20°C. The drag coefficient equations were implemented for various ranges of particle Reynolds number established a priori among those proposed in the literature by Folland (1988) and formulated starting from data published by Beard (1976) and Khvorostyanov and Curry (2005), hereinafter KC05.

The motion of particles when falling in the atmosphere is described by:

$$\rho_p V_p \boldsymbol{a}_\mathrm{p} = -\frac{1}{2}\, C_D A_p \rho_a (\mathbf{v}_p - \mathbf{v}_a)|\mathbf{v}_p - \mathbf{v}_a| + V_p(\rho_a - \rho_p)\boldsymbol{g} \tag{1}$$

where $\boldsymbol{a}_\mathrm{p}$ is the particle acceleration, $\mathbf{v}_a$ and $\mathbf{v}_p$ are the velocity vectors of the air and the particle, $\boldsymbol{g}$ is the gravity acceleration, $C_D$ is the drag coefficient, $A_p$ is the particle cross section area and $\rho_a$ and $\rho_p$ are the density of the air and the particle. Equation 1 assumes an upward positive orientation of the z axis, while the velocity and acceleration components are positive in the positive direction of the related axes. The quantity $\mathbf{v}_p - \mathbf{v}_a$ is the relative particle-to-air velocity.

The drag coefficient ($C_D$) is a dimensionless quantity used to represent the aerodynamic resistance of an object in motion in a fluid, such as air or water, and depends on the cross-sectional area of the object ($A_p$). The estimation of the drag coefficient is not easy. In the literature, different experiments were carried out with hydrometeors falling through the atmosphere with the objective of identifying suitable relationships between the drag coefficient and the particle dimension and/or its terminal velocity. Beard (1976) derived the $C_D$ by performing experiments in stagnant air, and measuring the dimension $d$ [mm] of the drops and their fall velocity $w_T$ [m s$^{-1}$].

When a particle falls in a stagnant air its Reynolds number is expressed as:

$$Re_p = \frac{w_T d}{\upsilon_a} \tag{2}$$

where $\upsilon_a$ is the air viscosity in m$^2$ s$^{-1}$. The drag coefficient is directly related to the Reynolds number of the particle in motion. When a particle is immersed in a flow field the equation 2 becomes a function of the particle-to-air velocity as follows:

$$Re_p = \frac{|\mathbf{v}_p - \mathbf{v}_a| d}{\upsilon_a} \tag{3}$$

Folland (1988) proposed different relationships between $Re_p$ and $C_D$, for various ranges of $Re_p$ (see equations 4 to 7) and assumed that the minimum value for $C_D$ must be fixed at 0.55.

$$Re_p < 0.01 \qquad C_D = 2547 \tag{4}$$

$$0.01 \le Re_p < 2 \qquad C_D = 1.06(24\, Re_p{}^{-1} + 2.400\, Re_p{}^{-0.045}) \tag{5}$$

$$2 \le Re_p \le 21 \qquad C_D = 1.06(24\, Re_p{}^{-1} + 2.640\, Re_p{}^{-0.19}) \tag{6}$$

$$21 < Re_p \qquad C_D = 1.06\left(24\, Re_p{}^{-1} + 4.536\, Re_p{}^{-0.368}\right) \tag{7}$$

The equations proposed by Folland (1988) provide terminal velocities of raindrops in still air at the temperature of 7.5°C and atmospheric pressure that agree to within 2% with those of Mason (1971) over the range of terminal velocities $0.1<w_T<8.3$ m s$^{-1}$.

In the work of KC05, different formulations of $C_D$, as a function of $Re_p$ obtained from experimental studies and analytical models, were summarized. Some of the curves proposed by KC05 are derived for spherical particles and other for crystals. The authors also introduce a correction, when the particle Reynolds number exceeds the value of $10^3$, in order to account for the turbulence effect due to the flow.

The $C_D$ values proposed by KC05 as a function of $Re_p$, for spherical particles in turbulent conditions, were fitted here for $Re_p > 60$ (approximately corresponding to a spherical drop of $d$ = 1 mm falling in air, with $\upsilon_a$= 1.5 $10^{-5}$ m$^2$s$^{-1}$, at an indicative fall velocity of 1 m s$^{-1}$) with an inverse first-order equation (Eq. 8). The values of the three parameters are $y_0 = 0.442$, $a = 3.402$, $b = 21.383$ and the correlation factor ($R^2$) is equal to 0.996.

$$C_D = y_0 + \frac{(a\ b)}{b + Re_p} \tag{8}$$

As shown in Figure 2, also the relationships proposed by Folland (1988) (black line) were compared with the raw data provided by KC05 (diamond). Based on this comparison the best-fit curve reported in Eq. 8 (grey line in Figure 2) was implemented in the LPT model to calculate the drag coefficient for $Re_p > 400$, while the equations proposed by Folland (1988) were adopted for $Re_p < 400$.

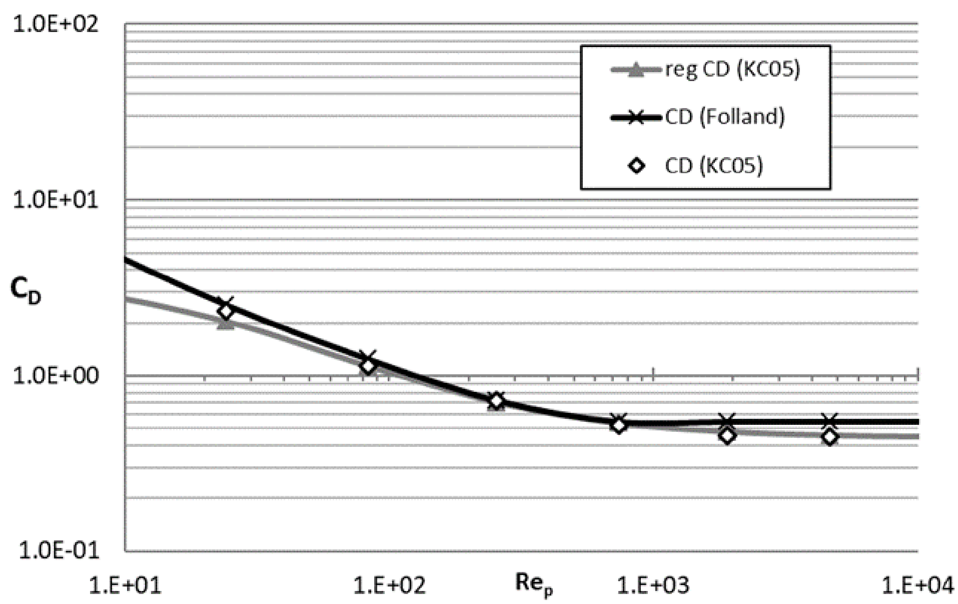


**Figure 2.** Comparison between the raw data proposed by KC05 (diamond), the best-fit curve of Equation 8 (grey line) and the formulation proposed by Folland (1988) (black line).

# 3 Results and discussion

## 3.1 CFD simulation results and validation

The performed CFD simulations confirmed previous literature results (e.g. Colli et al., 2018 and Cauteruccio, 2020): for both gauge geometries the airflow accelerates above the collector and significant updraft is obtained just in front of the gauge collector and above it. The region of maximum acceleration for the *Geonor T200B*© gauge shows higher values and is larger and more dispersed upward if compared with the aerodynamic response of the *Lambrecht Rain[e]H3* gauge. The maximum normalized updraft $U_z/U_{ref}$ occurs above the upwind edge of the collector and, e.g. at $z/D$ = 0.125, equals 0.65 and 0.50 for the *Geonor T200B*© and the *Lambrecht Rain[e]H3* gauge, respectively. These airflow features are the most influential on the hydrometeor trajectories, which are deflected upward due to the updraft and tend to be dragged beyond the collector when falling through the accelerated zone, where the horizontal velocity is larger than the undisturbed wind speed.

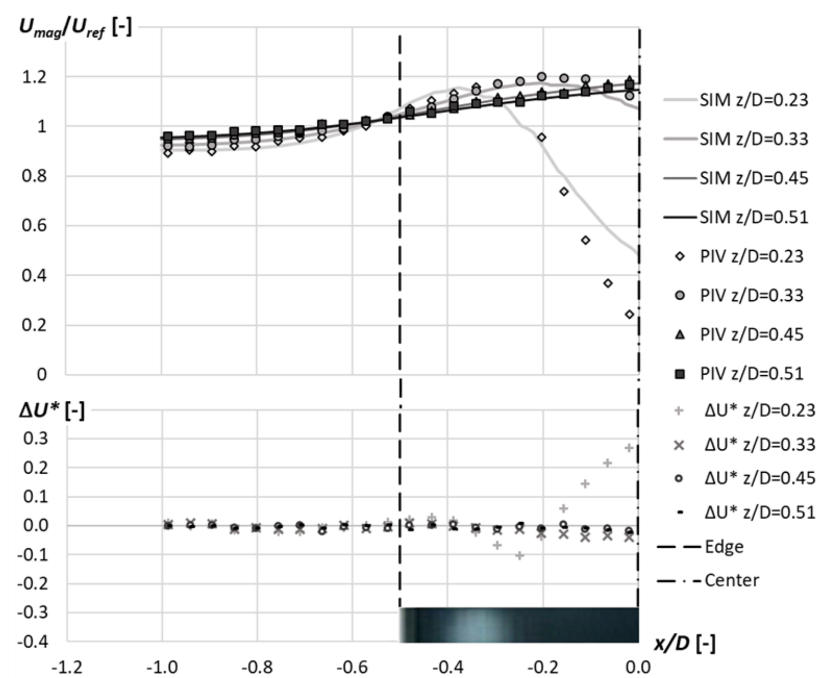


**Figure 3.** Comparison between URANS velocity profiles (continuous lines) and PIV measurements (markers) of the normalized magnitude of flow velocity ($U_{mag}/U_{ref}$) at $U_{ref}$ = 10 m/s and at different elevations along the central plane ($y/D$ = 0) of the *Geonor T200B*© gauge (top panel) and their absolute difference $\Delta U^*$ (bottom panel).

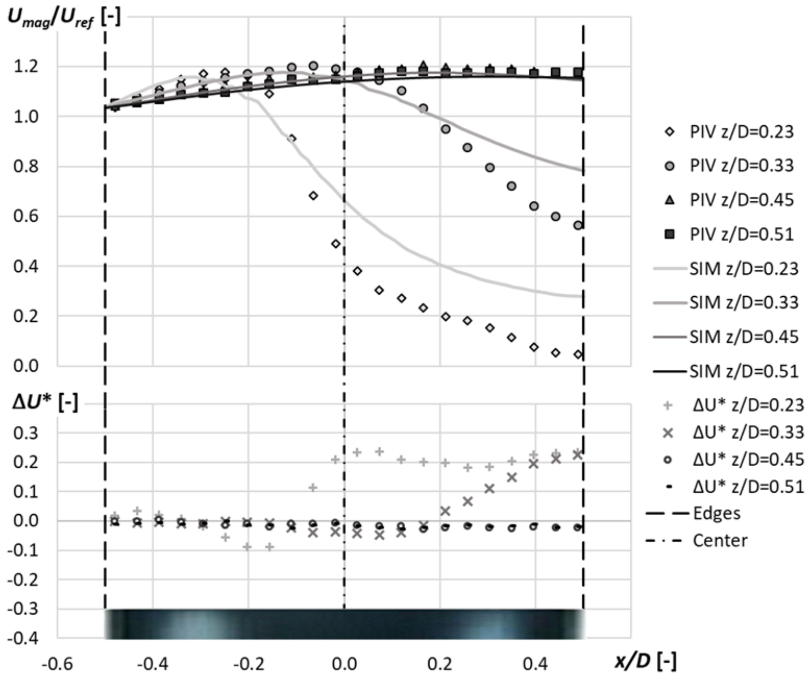


**Figure 4.** Comparison between URANS velocity profiles (continuous lines) and PIV measurements (markers) of the normalized magnitude of flow velocity ($U_{mag}/U_{ref}$) at $U_{ref}$ = 10 m/s and at different elevations along the plane *y/D* = 0.25 of the *Geonor T200B*© gauge (top panel) and their absolute difference $\Delta U^*$ (bottom panel).

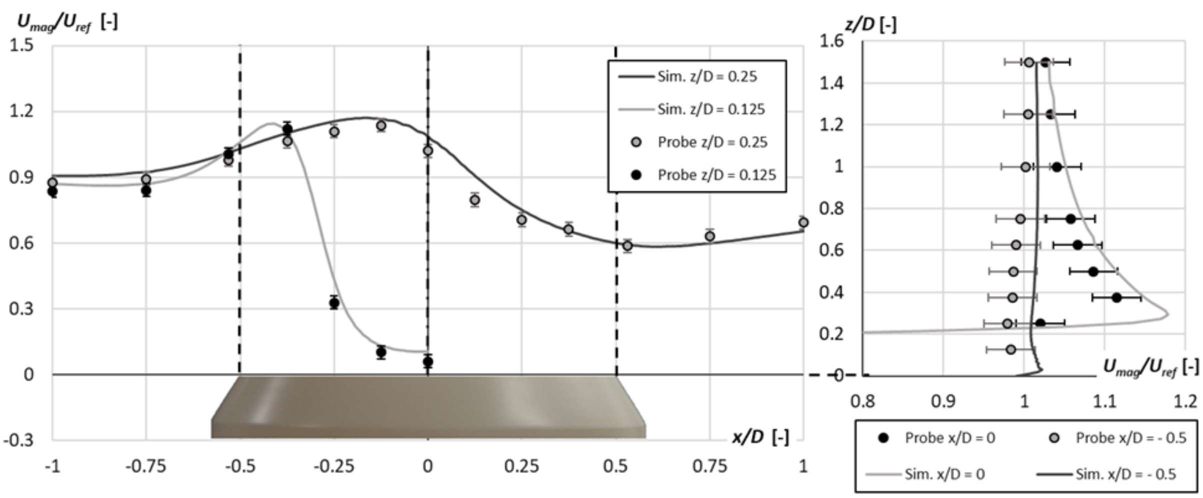


**Figure 5.** Comparison between URANS velocity profiles (continuous lines) and *Cobra* probe velocity measurements (circles with uncertainty bars) of the normalized magnitude of flow velocity ($U_{mag}/U_{ref}$) at $U_{ref}$ = 10 m/s in the central plane (*y/D* = 0) along two longitudinal sections at different elevations *z/D* (left-hand panel) and along two vertical sections in the upwind edge (*x/D* = - 0.5) and in the center (*x/D* = 0) of the collector (right-hand panel) for the *Lambrecht Rain[e]H3*© gauge.

Validation of the performed simulations was obtained in the WT using PIV and *Cobra* probe measurements. The comparison between PIV measurements and CFD longitudinal profiles of the normalized magnitude of the flow velocity at $U_{ref}$ = 10 m s$^{-1}$ for the *Geonor T200B*© gauge are reported in Figure 3 and Figure 4. The plots refer to different elevations (*z/D*) and vertical sections, at *y/D* = 0 and *y/D* = 0.25, respectively, and the absolute difference ($\Delta U^*$) between the measured and calculated values is also reported. An overall good agreement of the simulated profiles with measurements is obtained. The maximum differences occur at the minimum elevation where PIV measurements are available (*z/D* = 0.23) and range between 0.2 and 0.3. This is due the coarse discretization of the measured spatial domain, which introduces a smoothing effect on the measured flow field. Moreover, close to the gauge, measurements are still slightly affected by the reflection of the laser beam on the gauge rim, partially concealing the passive tracer from detection despite a mask was implemented to reduce such effect.

For the *Lambrecht Rain[e]H3*© four velocity profiles were sampled above the collector, along the longitudinal symmetry plane (*y/D* = 0) of the gauge, by employing a *Cobra* probe. The comparison between the local flow velocity measurements (circles) and numerical results (solid lines) are shown in Figure 5. The longitudinal profiles were measured at *z/D* = 0.125 and *z/D* = 0.25, while the vertical profiles at the center and the upwind edge of the collector (*x/D* = -0.5 and *x/D* = 0). In all cases, the numerical profiles fall within the uncertainty of the probe measurements, depicted with bars, confirming the good quality of the adopted CFD setup.

### 3.2 Observation of the deflected trajectories

For the two investigated gauges, a few sets of drops captured in the GVPM WT when travelling above the gauge collector are shown in this section, and the observed trajectories are commented according to the aerodynamic response of the gauge body. Drop trajectories are depicted in the dimensionless plane (*x/D*, *z/D*), where the gauge collector is centered in (0, 0) and the longitudinal coordinate, *x/D*, of the drop releasing position is fixed, while its elevation, *z/D* assumed positive downward, varies with the wind speed. In the legend, the prefix in the coding of each trajectory indicates the name of the gauge under test (G for *GeonorT200B*© and L for *Lambrecht Rain[e]H3*©).

Overall, the experimental campaign in the WT resulted in the capturing of 82 trajectories of drops released between z/D = -0.05 and z/D = -0.7 above the *GeonorT200B*©, at $U_{ref}$ = 8.86 to 13.6 m s$^{-1}$, and 106 trajectories of drops released between z/D = -0.18 and z/D = -0.7 above the *Lambrecht Rain[e]H3*©, at $U_{ref}$ = 8.9 to 13.1 m s$^{-1}$.

Two sample sets of drop trajectories shot at 1000 and 10 fps are shown in Figure 6 (left and right panel, respectively), as observed above the collector of the cylindrical and chimney shaped gauges at $U_{ref}$ = 12.5 m s$^{-1}$ and $U_{ref}$ = 11.4 m s$^{-1}$, respectively. The particle-fluid interaction above the collector of the gauges is responsible for a significant deviation of the trajectories, and this can be observed here for all trajectories when travelling beyond the upwind edge of the collector (*x/D* = -0.5). In both cases, a few undisturbed trajectories aiming at entering the collector close to the downwind edge (*x/D* = 0.5) overtake its rim and fall outside of the gauge. The shooting of the deviated trajectories in the WT allowed clear visualization of the wind-induced undercatch by showing that some drops actually fall outside instead of inside of the collector, contrary to what would be expected by following their undisturbed trajectory.

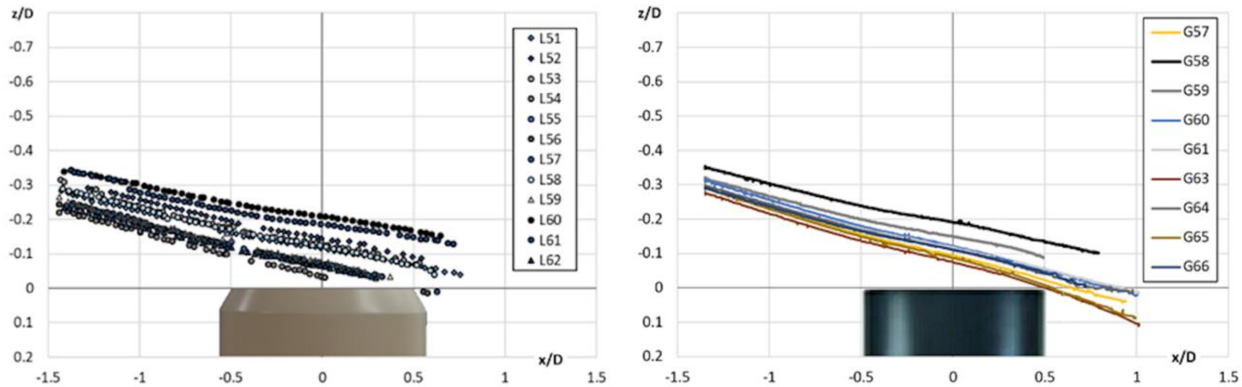


**Figure 6.** Sample sets of drop trajectories shot at 1000 (left) and 10 (right) fps, as observed above the collector of the cylindrical and chimney shaped gauges at $U_{ref}$ = 12.5 m s$^{-1}$ and $U_{ref}$ = 11.4 m s$^{-1}$, respectively.

The estimated undisturbed trajectory is added in the top panel of Figure 7 (dashed line) for one sample drop travelling above the *Lambrecht Rain[e]H3*© gauge at $U_{ref}$ = 12.5 m s$^{-1}$. In this case, the observed trajectory starts detaching from the undisturbed one when its longitudinal coordinate reaches the upwind edge of the collector (at about *x/D* = - 0.5), where the airflow updraft is most significant (as reported by Cauteruccio, 2020).

The observed drop trajectory was elaborated by linearly interpolating the positions associated with the undisturbed part of the trajectory, while the disturbed part was fitted with a third order polynomial. In Figure 7 (top panel), the undisturbed part of the observed trajectory is painted with a dark grey while the disturbed part is painted in light grey and the interpolation curves are marked with dots. The threshold between the undisturbed and disturbed part of the trajectory was obtained by adopting a trial and error procedure with the objective to ensure the continuity of the slope curve (*z/x*) obtained as the first derivative of the fitted trajectory (Figure 7, bottom panel).

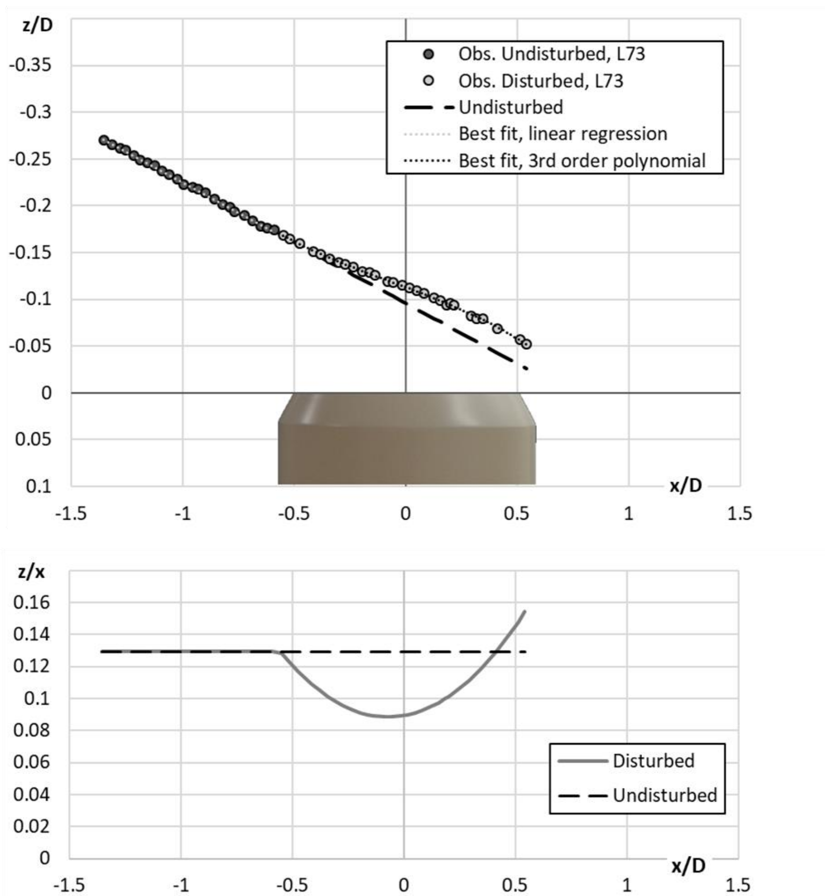


**Figure 7.** Observed (circles) and undisturbed (dashed line) drop trajectory above the collector of the gauge with cylindrical shape (top panel) at $U_{ref}$ = 12.5 m s$^{-1}$, and the associated slope curves for both trajectories (bottom panel).

Two drop trajectories, identified with the names G8 and G9, travelling above the collector of the *Geonor T200B*© gauge at $U_{ref}$ = 10.2 m s$^{-1}$ are depicted in Figure 8. The initial elevation (*z/D*) of the two droplets is not much different. The initial, undisturbed part of the slope curve reveals that the two droplets have a similar size, while the drop starting at a higher elevation is deviated a bit later following the airflow pattern. The difference between the observed and undisturbed trajectories, red markers with scale on the right-hand axis, is larger in the second half part of the collector where the two droplets are dragged beyond the gauge, resulting in some undercatch.

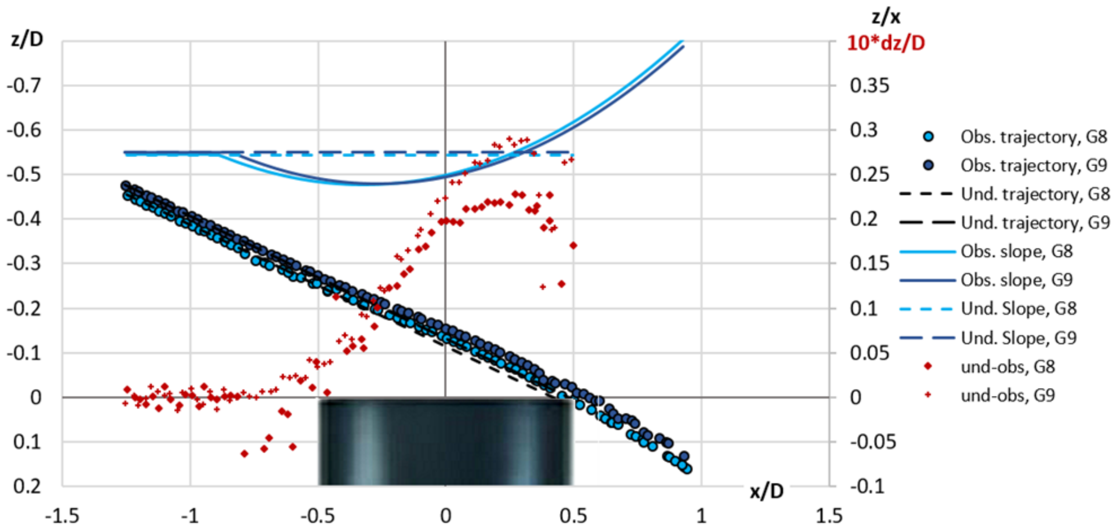


**Figure 8.** Comparison of two drop trajectories (circles) having similar size, travelling above the collector of the chimney shaped gauge at $U_{ref}$ = 10.2 m s$^{-1}$, together with the associated undisturbed trajectories (dashed lines). The associated slope curves (scale on the right-hand axis) are shown with colored solid and dashed lines for the disturbed and undisturbed trajectories, respectively. Red markers represent the difference between the observed and undisturbed trajectories in terms of normalized vertical coordinates (scale on the right-hand axis).

## 3.3 Validation of the Lagrangian Particle Tracking model

The validation of the LPT model was obtained by comparison between observed and simulated trajectories. In the numerical model the initial conditions, normalized position (*x/D* and *z/D*) and velocity components (*u* and *w* [m s$^{-1}$], the latter assumed positive downward), of the simulated trajectories were set consistently with the WT observations. CFD airflow velocity fields were rescaled according to the free-stream velocity value used in the WT. The initial velocity components were set equal to the mean values of the three to five initial positions of each drop as shot by the camera, so as to avoid the noise due to the uncertainty in the initial positions. The drop diameter, *d*, which has a major role in the calculation of the drop trajectory by affecting $Re_p$ and therefore $C_D$, is obtained here as a calibration parameter for each trajectory, since the drop releasing mechanism and the acquisition system cannot provide sufficient accuracy in the assessment of the drop size. The initial conditions of the drop trajectories used in the validation phase and their estimated diameter are listed in Table 1. A few examples of simulated drop trajectories, compared with the observed ones, are presented and discussed in this section to support the validation phase.

The observed (circles) and simulated (solid line) patterns of the drop trajectory identified with the name G2, are compared in Figure 9. The maximum difference between the vertical positions (*z* in mm), computed at each normalized longitudinal coordinate (*x/D*) of the observed trajectory, arises at the upwind edge of the collector and is about 1.2 mm. This difference is comparable with the drop size (see Table 1), therefore with the uncertainty in the assessment of the drop position, identified as a bright moving object in each frame. The calculated horizontal acceleration of the drop, normalized with the one experienced in the initial undisturbed part of the trajectory, is also shown (scale on the right-hand axis). Consistently with the PIV airflow velocity fields, the drop significantly accelerates when travelling above the upwind part of the collector, where the airflow is indeed accelerated, until crossing the separation layer between the airflow recirculation and accelerated zones, when it starts decelerating abruptly towards the downwind edge of the collector.

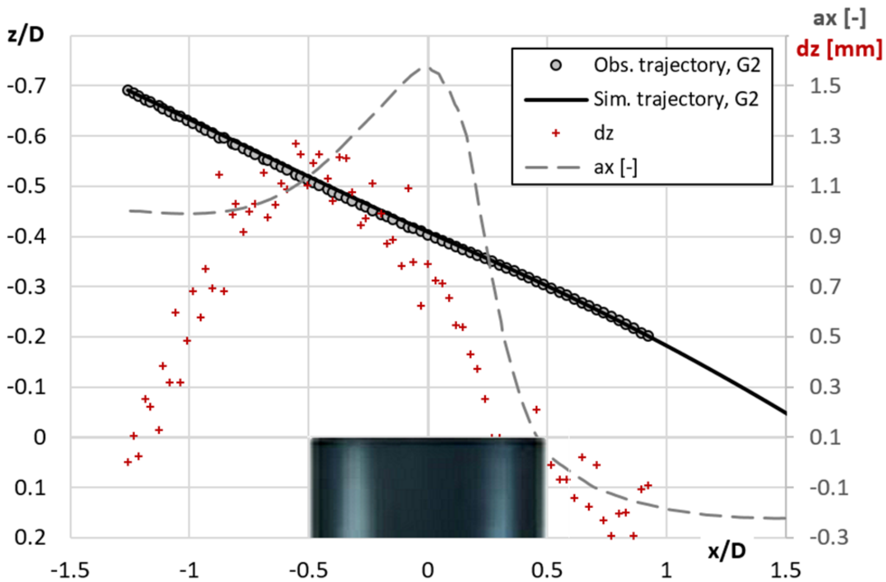


**Figure 9.** Observed (circles) and simulated (solid line) drop trajectories above the collector of a chimney shaped gauge at $U_{ref}$ = 10.2 m s$^{-1}$. The difference *dz* (mm) between the observed and simulated vertical coordinates of the drop trajectories (red crosses) at each normalized observed longitudinal coordinate (*x/D*) is reported (scale on the right-hand axis), together with the numerical longitudinal acceleration ($a_x$) of the drop (dashed line).

The good repeatability of the trajectories of very similar drops in the WT (see their estimated size in Table 1) is shown in Figure 10. By injecting drops of the same size in the WT, the observed trajectories are indeed very close to each other, and they experience very similar deviations above the collector. Moreover, simulated trajectories show that the LPT model is able to replicate even the small variations due to slight differences in the initial conditions about the drop velocity.

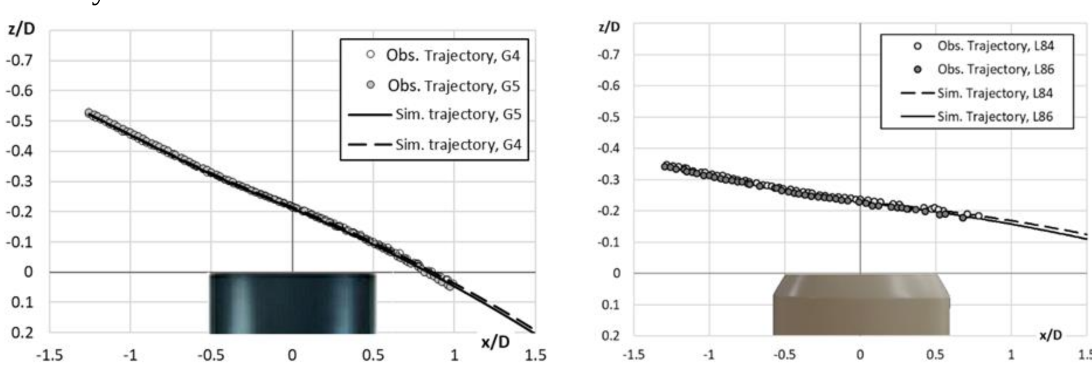


**Figure 10.** Pairs of drops having approximately the same size travelling above the collector of a chimney shaped gauge at $U_{ref}$ = 10.2 m s$^{-1}$ (left-hand panel) and a cylindrical gauge at $U_{ref}$ = 13.1 m s$^{-1}$ (right-hand panel). Observed (circles) and simulated (lines) trajectories are depicted for the two pairs of drops.

The observed drop trajectories G8 and G9, already shown in Figure 8, are compared with the simulated trajectories in **Figure 11**. As already noted, the two droplets have the same size; this assumption is confirmed by the obtained numerical trajectories because the optimal agreement between the observed and simulated trajectories is reached by setting the drop diameter equal to one millimeter. Also in this case, the difference between observed and simulated trajectories is comparable with the uncertainty in the assessment of the drop position, given the dimension of the drop (see Table 1) and the image resolution. The vertical acceleration of the drops ($a_z$) obtained from the simulation, normalized with the one experienced in the initial undisturbed part of the trajectory, is depicted with dashed lines: the two drops accelerate when reaching the upwind edge of the collector, due to the updraft, and then decelerate. This behavior is in line with the measured PIV velocity field where, beyond $x/D$ = -0.25, the updraft zone is always located above the normalized elevation $|z/D|$ = 0.2 and the two drops are fully immersed in the recirculation zone.

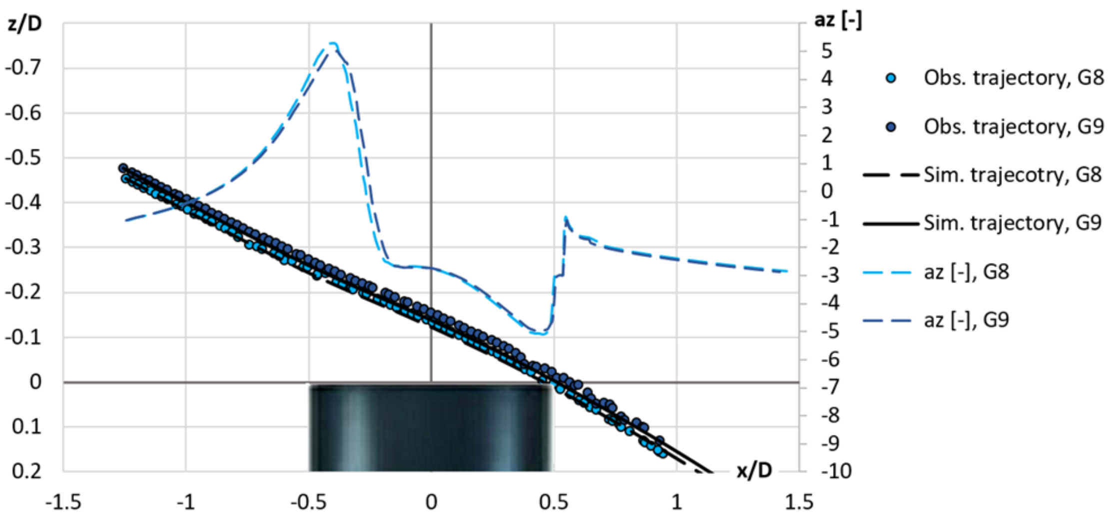


**Figure 11**. Comparison of two simulated and observed trajectories for two drops travelling above the collector of the chimney shaped *Geonor*© gauge at $U_{ref}$ = 10.2 m s$^{-1}$, together with the simulated profiles of their normalized vertical acceleration (scale on the right-hand axis).

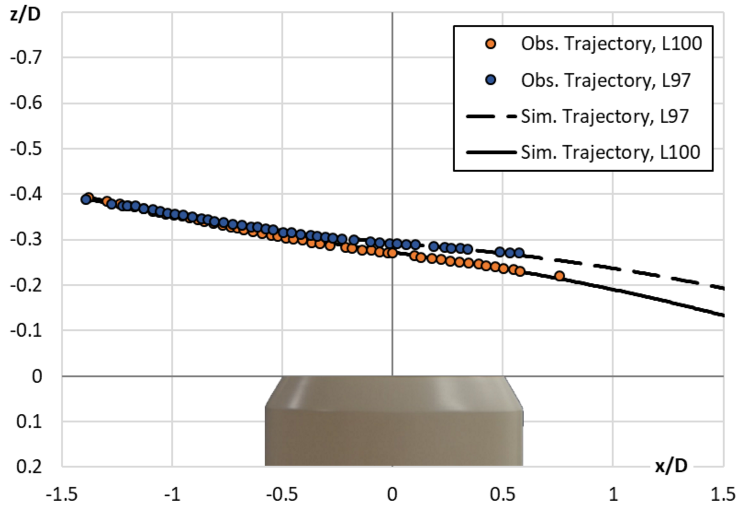


**Figure 12**. Observed (circles) and simulated (lines) drop trajectories for two drops released at the same initial position travelling above the collector of the cylindrical gauge at $U_{ref}$ = 13.1 m s$^{-1}$.

Observed and simulated patterns are depicted in **Figure 12** for a pair of drop trajectories (named L97 and L100) having different drop size (*d* = 0.7 and 0.9) but being released at the same initial position. As reported in Table 1, also the values of the initial velocity components are very similar. The lighter drop has a lower slope and is maintained at a higher elevation along the entire trajectory. As revealed by the PIV velocity field, this is due to the persistence of updraft velocity components above |*z/D*| = 0.25 within the limits of the collector, while below this vertical coordinate the separation layer occurs and downward vertical velocity components arise.

**Table 1.** WT flow velocity, initial coordinates and velocity components for the simulated drop trajectories and the resulting drop diameter.

| ID | Wind [m s$^{-1}$] | *x/D* | *z/D* | u [m s$^{-1}$] | w [m s$^{-1}$] | *d* [mm] |
|---|---|---|---|---|---|---|
| G2 | 10.2 | -1.259 | -0.690 | 4.286 | 0.952 | 1.2 |
| G4 | 10.2 | -1.257 | -0.523 | 4.140 | 1.104 | 1.0 |
| G5 | 10.2 | -1.257 | -0.523 | 4.122 | 1.122 | 1.0 |
| G8 | 10.2 | -1.247 | -0.455 | 4.048 | 1.190 | 1.0 |
| G9 | 10.2 | -1.256 | -0.477 | 3.968 | 1.190 | 1.0 |
| L84 | 13.1 | -1.280 | -0.349 | 5.571 | 0.667 | 0.7 |
| L86 | 13.1 | -1.293 | -0.343 | 5.801 | 0.602 | 0.7 |
| L97 | 13.1 | -1.392 | -0.389 | 5.855 | 0.482 | 0.7 |
| L100 | 13.1 | -1.379 | -0.393 | 5.667 | 0.524 | 0.9 |

Validation of the coupled CFD and LPT approach was obtained after numerically simulating about 25 trajectories of drops released in the WT experiment. A synthesis of the validation performance is reported in Table 2 The maximum, mean and median difference, *dz*, between the vertical coordinates along each observed and simulated trajectory, normalized with the estimated drop diameter, *d*, were calculated as suitable performance parameters. For each of them, the maximum, minimum, mean and standard deviation values obtained over the set of all trajectories used in the validation exercise are listed in Table 2. The same statistics are included for the root mean square difference between the observed and simulated vertical coordinates along each trajectory.

The validation was satisfactory since the mean of the maximum differences between the simulation and the observed trajectory is about unity, with a low standard deviation (the coefficient of variation is about 0.4). Also, the mean and median values of *dz* are very similar, showing a symmetrical spread of these differences around the perfect agreement, which suggests quite a random nature of the error. Finally, the RMSD is very low, always below $10^{-3}$, indicating an overall good agreement for all pairs of simulated and observed trajectories.

**Table 2.** Validation statistics for the selected performance parameters

| | Max (dz/d) | Mean (dz/d) | Median (dz/d) | RMSD |
|---|---|---|---|---|
| Max | 2.1492 | 1.0444 | 1.2154 | 0.000812 |
| Min | 0.1871 | -0.4230 | -0.4946 | 0.000213 |
| Mean | 1.0968 | 0.0332 | 0.0337 | 0.000429 |
| Std dev | 0.4351 | 0.3514 | 0.3905 | 0.000168 |

## 4 Conclusions

Although the experimental conditions here implemented in the WT were forcedly different from reality (constant and low turbulence airflow), and the initial conditions of the drops at their releasing position were different from those expected in the natural environment (null horizontal and vertical velocity instead of the free-stream and terminal velocity, respectively), the performed validation of the coupled CFD and LPT approach on a physical full-scale model supports its application in realistic simulation scenarios.

Typically, applications include the numerical calculation of the collection efficiency of precipitation gauges having different outer geometries (based on suitable assumptions about the hydrometeors characteristics, drag coefficient and drop size distribution) to derive adjustment curves for the wind-induced bias of precipitation measurements.

Previous works on this subject mostly concentrated on field studies based on the comparison of measurements obtained from shielded and unshielded gauges, and adjustment curves (also termed transfer functions) were derived from field data alone, assuming some gauge/windshield configuration as a reference. Limitations of the empirical approach include the high variability of the hydrometeor microphysical characteristics in precipitation events

(Thériault et al., 2012), as well as the possible wind-induced biases associated with the reference configuration (Thériault et al., 2015). The resulting large spread of field data around the interpolating curves suggests that important driving factors are understated, such as precipitation intensity and/or the particle size distribution, as recently shown by Colli et al. (2020).

The present work aims at overcoming these existing gaps, to shed additional light on the wind exposure problem and to achieve results that can be used operationally to adjust precipitation measurements when these are obtained in windy conditions. Indeed, the WT validation of the numerical approach based on CFD and LPT simulations support its use as the theoretical basis for the interpretation of the wind-induced bias of field measurements obtained from shielded and unshielded precipitation gauges. Field measurements from suitable test sites, equipped with reference gauges in the appropriate configuration, remains essential to provide the real-world test bench and calibration basis needed to confirm the parameterization adopted (e.g. for the drag coefficient) in the theoretical approach.

## Acknowledgments and Data

This work was developed in the framework of the Italian national project PRIN20154WX5NA "Reconciling precipitation with runoff: the role of understated measurement biases in the modelling of hydrological processes", and as partial fulfilment of the PhD thesis of the first author. The coordinates of the observed drop trajectories used in this work are available online at http://www.precipitation-biases.it/ Drop-Trajectories-WRR.php

## References

Beard, K.V. (1976). Terminal velocity and shape of cloud and precipitation drops aloft. *Journal of the Atmospheric Sciences*, *33*, 851–864. https://doi.org/10.1175/1520-0469(1976)033%3C0851:TVASOC%3E2.0.CO;2

Cauteruccio, A. (2020). The role of turbulence in particle-fluid interaction as induced by the outer geometry of catching-type precipitation gauges. (Ph.D. Thesis). Ph.D. course in Civil, Chemical and Environmental Engineering, curriculum in Fluid Dynamics and Environmental Engineering, Unversity of Genoa. https://doi.org/10.15167/cauteruccio-arianna_phd2020-04-06.

Cauteruccio, A., Colli, M., Freda, A., Stagnaro, M. & Lanza, L.G. (2020). The role of the free-stream turbulence in attenuating the wind updraft above the collector of precipitation gauges. *Journal of Atmospheric and Oceanic Technology*, *37* (1), 103–113. https://doi.org/10.1175/JTECH-D-19-0089.1

Colli, M., Lanza, L.G., Rasmussen, R., Thériault, J.M., Baker, B.C. & Kochendorfer, J. (2015). An improved trajectory model to evaluate the collection performance of snow gauges. *Journal of Applied Meteorology and Climatology*, *54*, 1826–1836. https://doi.org/10.1175/JAMC-D-15-0035.1

Colli, M., Lanza, L.G., Rasmussen R. & Thériault, J.M. (2016a). The collection efficiency of shielded and unshielded precipitation gauges. Part I: CFD airflow modelling. *Journal of Hydrometeorology*, *17*, 231–243. https://doi.org/10.1175/JHM-D-15-0010.1

Colli, M., Lanza, L.G., Rasmussen R. & Thériault, J.M. (2016b). The collection efficiency of unshielded precipitation gauges. Part II: modeling particle trajectories. *Journal of Hydrometeorology.*, *17*, 245–255. https://doi.org/10.1175/JHM-D-15-0011.1

Colli, M., Pollock, M., Stagnaro, M., Lanza, L.G., Dutton, M., & O'Connell, P.E. (2018). A Computational Fluid-Dynamics assessment of the improved performance of aerodynamic raingauges. *Water Resources Research, 54*, 779–796. https://doi.org/10.1002/2017WR020549

Colli, M., Stagnaro, M., Theriault, J.M., Lanza, L.G. & Rasmussen, R. (2020). Adjustments for Wind- Induced Undercatch in Snowfall Measurements based on Precipitation Intensity. *Journal of Hydrometeorology*, *21*(5), 1039–1050. https://doi.org/10.1175/JHM-D-19-0222.1

Constantinescu, G.S., Krajewski, W.F., Ozdemir, C. & Tokyay, T. (2007). Simulation of airflow around rain gauges: comparison of LES with RANS models. *Advances in Water Resources.*, *30*, 43–58. https://doi.org/10.1016/j.advwatres.2006.02.011

Folland, C.K. (1988). Numerical models of the raingauge exposure problem, field experiments and an improved collector design. *Quarterly Journal of the Royal Meteorological Society, 114*, 1485–1516. https://doi.org/10.1002/qj.49711448407

Green, M.J. & Helliwell, P. R. (1972). The effect of wind on the rainfall catch. Distribution of precipitation in mountainous areas, World Meteorological Organization, Rep. 326, Vol. 2, 27–46.

Jones, W.P. & Launder, B.E. (1972). The prediction of laminarization with a two-equation model of turbulence. *International Journal of Heat and Mass Transfer, 15*, 301–314. https://doi.org/10.1016/0017-9310(72)90076-2

Khvorostyanov, V.I. & Curry, J.A. (2005). Fall Velocities of Hydrometeors in the Atmosphere: Refinements to a Continuous Analytical Power Law. *Journal of the Atmospheric Sciences, 62*, 4343–4357. https://doi.org/10.1175/JAS3622.1

Mason, B.J. (1971). The Physics of Clouds. 2nd edition, Clarendon Press. ISBN: 9780199588046

Menter, F. (1993). Zonal two equation k-ω turbulence models for aerodynamic flows. AIAA 24th Fluid Dynamics Conference, 93, p.2906. https://doi.org/10.2514/6.1993-2906

Mueller, C.C. & Kidder, E.H. (1972). Rain gage catch variation due to airflow disturbances around a standard rain gage. *Water Resources Research, 8*(4), 1077-1082. https://doi.org/10.1029/WR008i004p01077

Nešpor, V. & Sevruk, B.(1999). Estimation of wind-induced error of rainfall gauge measurements using a numerical simulation. *Journal of Atmospheric and Oceanic Technology, 16* (4), 450 - 464. https://doi.org/10.1175/1520-0426(1999)016%3C0450:EOWIEO%3E2.0.CO;2

Rasmussen, R., Vivekanandan, J., Cole, J. & Masters, B.M.C. (1999). The estimation of snowfall rate using visibility. *Journal of Applied Meteorology, 38* (10), 1542–1563. https://doi.org/10.1175/1520-0450(1999)038%3C1542:TEOSRU%3E2.0.CO;2

Robinson, A.C. & Rodda, J.C. (1969). Rain wind and aerodynamic characteristics of rain-gauges. *Meteorological Magazine, 98*, 113-120.

Thériault, J.M., Rasmussen, R., Ikeda, K. & Landolt, S. (2012). Dependence of snow gauge collection efficiency on snowflake characteristics. *Journal of Applied Meteorology and Climatology*, *51*, 745–762. https://doi.org/10.1175/JAMC-D-11-0116.1

Warnik, C.C. (1953). Experiments with windshields for precipitation gages. *Transactions of the American Geophysical Union*, *34*(3), 379 - 388. https://doi.org/10.1029/TR034i003p00379

Wilcox, D. C. (1988). Reassessment of the scale-determining equation for advanced turbulence models. *AIAA journal*, *26*(11), 1299–1310. https://doi.org/10.2514/3.10041

Wilcox, D.C. (2006). Turbulence Modeling for CFD. D C W Industries, 3rd edition.